# Refractive index engineering by fast ion implantations: a generic method for constructing multi-components electro-optical circuits

Aharon J. Agranat, Alexander Gumennik and Harel Ilan
Department of Applied Physics, The School of Engineering and Computer Science,
The Hebrew University, Jerusalem 91904, ISRAEL.

## ABSTRACT

Refractive index engineering (RI_Eng) by ion implantations is a generic methodology for constructing multi-component integrated circuits of electrooptic and nanophotonic devices with sub-wavelength features operating in the visible - near IR wavelengths. The essence of the method is to perform spatially selective implantations for sculpting complex 3D pre-designed amorphized patterns with sub-wavelength features and reduced refractive index within the volume of the substrate. A number of devices that were constructed in a substrate of potassium lithium tantalate niobate are described, including a submerged slab waveguide, an optical wire and a channel waveguide array.

**Keywords**: integrated optoelectronic circuits, electrooptical materials, microstructure fabrication, ion implantation, ferroelectric materials, KLTN.

## 1. INTRODUCTION

It is well known that the implantation of high energy ions in crystalline substrates causes partial amorphization at a well localized layer within the depth of the substrate. Furthermore, the refractive index (RI) in the amorphized layer becomes substantially different than the RI in the surrounding crystalline material. Refractive Index Engineering (RI_Eng) is a technique for sculpting complex 3D structures with sub-micron features that is based on these phenomena.

The essence of RI_Eng is to define the shape of the amorphized regions by controlling the spatial distribution of the amorphization. This is accomplished by allowing the implanted ions to penetrate the substrate to be limited to predefined areas using blocking masks to prevent their penetration elsewhere, and to set the depth at which the amorphization occurs by controlling the incident energy of the ions.

It is argued henceforth that RI_Eng has the necessary elements to become a generic method for constructing complex circuits in which electrooptical devices, optical components, and nanophotonic structures are integrated together in the same substrate, interconnected by a mesh of waveguides (WG) and operate in unison. In this paper the potential of RI_Eng as a generic fabrication method for such electrooptical circuits will be described, demonstrated, and discussed.

The electrooptical substrate that was chosen to explore the potential of RI_Eng is potassium lithium tantalate niobate (KLTN). Although in principle RI_Eng can be implemented in a wide range of electrooptical substrates, KLTN was found to be an especially attractive substrate for this purpose. KLTN is an oxygen perovskite crystal with a composition given by $K_{1-x}Li_xTa_{1-y}Nb_yO_3$. KLTN becomes ferroelectric at a temperature $T_c$ determined by the relative concentrations of Nb with respect to Ta, and Li with respect to K respectively. In particular it was found that for very low concentration of Li ($x<<1$) and $y>0.2$, $T_c$ is given by: $T_c \approx 682+33.2y$ K. Above $T_c$ KLTN is paraelectric and exhibit a quadratic electrooptic effect given by

$$\Delta n = \left(\frac{1}{2}\right) n_0^3 g_{eff} P^2 \tag{1}$$

where $\Delta n$ is the induced change in the RI, $n_o$ is the RI at the paraelectric phase, $g_{eff}$ is the effective quadratic electrooptic coefficient which depends on the relative orientation of the polarization of the propagating beam with respect to the crystallographic axes of the crystal, and P is the electrical induced polarization. At the paraelectric phase: $P=\varepsilon_o(\varepsilon_r-1)E \approx \varepsilon E$ where E is the applied electric field and it is assumed that $\varepsilon_r>>1$. The quadratic electrooptical tensor of KLTN at the paraelectric phase is a fourth rank tensor given by $\mathbf{g}=(g_{ijkl})$ where $g_{11}=g_{iiii}= 0.16$ m$^4$/C$^2$; $g_{12}=g_{ijij}= -0.02$ m$^4$/C$^2$ i≠j; $g_{44}=g_{iijj}= 0.08$ m$^4$/C$^2$ i≠j. Thus, a beam propagating along the crystallographic [001] axis polarized along the crystallographic [010] axis in a crystal for which $\varepsilon_r=3\cdot10^4$ will experience, subject to the application of an electric field of $E=3\cdot10^3$ V/cm collinear with the polarization so that $g_{eff.}=g_{11}=0.16$ m$^4$/C$^2$, a change in the RI given by $\Delta n\approx0.01$. KLTN is grown in the bulk using the top seeding solution growth method [1]. We have recently found that high quality KLTN can also be grown by liquid phase epitaxial growth. Thin layers of KLTN can also be grown by Metalo Organic Chemical Vapor Deposition [2].

As can be seen KLTN manifests an especially strong electrooptic effect. KLTN doped with copper was found to be an especially attractive material for photorefractive applications such as Electroholography (EH). In EH applications, a switching time of approximately 10 nanosecond was demonstrated. It was also shown that electrooptical devices with a KLTN medium can be operated in the visible spectral range without developing space-charge induced optical damage if the devices are operated with bipolar driving voltages. This opens the way for constructing electrooptical circuits that operate in the visible down to ≈400nm.

## 2. THE PHYSICAL PRINCIPLES OF REFRACTIVE INDEX ENGINEERING

### 2.1 Physical mechanisms of Refractive Index Engineering

RI_Eng exploits the fact that the implantations of fast ions in a crystalline substrate create changes in the RI in well defined regions of the substrate. This process is illustrated schematically in Figure 1.

In general, the implantation of light ions in solid crystalline material is governed by two mechanisms, electronic stopping and nuclear stopping [3]. Upon penetrating the material the ions are dominated by the electronic stopping mechanism: due to their high initial velocity the ions do not interact with the lattice atoms, and continue to travel in their initial direction almost without affecting the medium in which they propagate. However, they do interact with the electronic clouds that surround the lattice ions. While they travel deeper into the lattice, these inelastic interactions cause them to slow down gradually with very little divergence from the initial propagation direction in a manner which is similar to experiencing a friction force, i.e. the stopping force is proportional to the velocity. As the implanted ions become slow enough their cross section for interaction with the lattice atoms increases steeply. i.e. the elastic collisions of the implanted ions with the atoms of the lattice become the dominant scattering mechanism. During this nuclear stopping phase the implanted ion tears out atoms from their original sites in the lattice forcing them to become interstitials at different sites, leaving behind vacancies. These interstitial atoms constitute lattice defects of the Frenkel type [4].

Let $E_n$ and $E_e$ be the energies deposited in nuclear collisions and electronic collisions respectively by the implanted ion as it traverses through the material, and let R be the distance traveled by the implanted ion into the material. Following the Lindhart-Scharff-Schiott (LSS) normalization procedure [5], it is customary to express $E_n$, $E_e$, and R by the normalized quantities $\varepsilon_n$, $\varepsilon_e$ and ρ respectively given by

$$\begin{aligned} \varepsilon &= \varepsilon_1 E = \left[\frac{M_2}{M_1+M_2}\cdot\frac{4\pi\varepsilon_0 a}{Z_1 Z_2 q^2}\right]E \\ \rho &= \rho_1 R = N\pi a^2\frac{4M_1M_2}{(M_1+M_2)^2}R \end{aligned} \tag{2}$$

where $M_1$, $M_2$ are the projectile ion and the target atom masses respectively, $Z_1$, $Z_2$ are atomic numbers of the projectile ion and the target atom respectively, q is the electron charge and a is the measure for interaction potential screening length which is given by $a = 0.8853 a_0 (Z_1^{2/3} Z_2^{2/3})^{-1/2}$ where $a_0$ is the Bohr radius. The LSS normalization is chosen in such a way that the nuclear stopping curve is universal in contrary to the electronic stopping slope which changes with the target properties and the species of the implanted ion.

The normalized nuclear stopping force $-d\varepsilon_n / d\rho$, and the electronic stopping forces $-d\varepsilon_e / d\rho$, for the case of $He^+$ ions implanted in a KLTN substrate, as derived by the TRIM simulation program [6], are presented in Figure 1 as function of the normalized penetration velocity $\varepsilon_e^{1/2}$. As can be seen, the electronic stopping force has the characteristics of a friction force, whereas the nuclear stopping force is a maximized at a specific penetration distance causing the Frenkel defects to be localized at a well defined depth within the substrate.

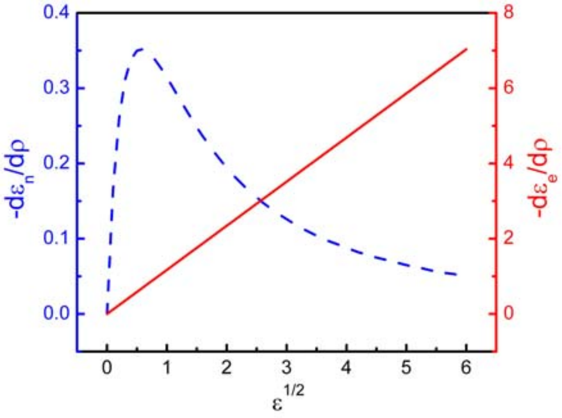

Figure 1. The nuclear stopping $-d\varepsilon_n / d\rho$ (dashed line), and the electronic stopping $-d\varepsilon_e / d\rho$ (solid line) as a function of the square root of the normalized energy in LSS units for He implanted in KLTN.

The Frenkel defects that are formed by the implantations constitute a layer of partially amorphized material in which the RI differs substantially from the RI in the surrounding lattice. Consider for example a KLTN substrate that was implanted by $He^+$ ions at 2.3 MeV with a dosage of $\approx 10^{16}$ ion/cm$^2$. The spatial distribution of the amorphization created by the implantation process derived by TRIM simulation is presented in Figure 3 [7]. As can be seen this implantation process created an amorphized layer peaked at 5μm with a width of 0.5 μm (defined as the full width at half the maximum (FWHM)).

In KLTN the RI in the amorphized region is lower than the RI in the crystalline regions. Thus, the structure formed by the implementation process in a KLTN substrate constitutes a slab WG in which the core is the crystalline layer immediately below the surface, cladded from above by air, and from below by the amorphized layer.

In particular, the WG created by the process described above was studied by measuring the dark mode spectrum using a prism coupler set-up operated at λ=1.3 μm. The results are shown in Figure 2. As can be seen this implementation process induced a peak reduction of the RI in the amorphized layer of approximately ~5%. Furthermore, as can be seen the RI profile that was derived from optical measurements using the method of Chandler & Lama [8] coincide with the distribution of the amorphization derived by the TRIM simulation. It was also found that immediately after the implantation the core of the slab WG contains a large concentration of electronic defects. These can be removed by annealing at a temperature below 200 °C. The propagation loss measured in the slab WG was found to be 0.1-0.2 dB/cm.

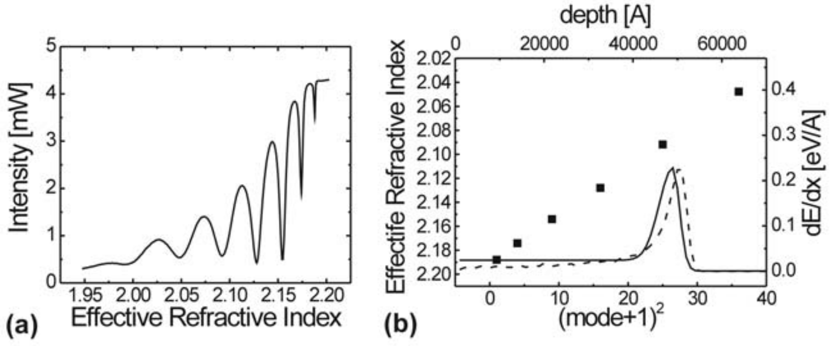

Figure 2. (a) TE reflection spectrum measured at λ=1.3 μm of the WG formed by the implantation of $He^+$ ions with energy of 2.26 MeV and dosage of $0.95\cdot 10^{16}$ ion/$cm^2$; (b) the WG RI profile at λ =1.3 μm shown together with the effective indices of the respective propagation modes: RI profile reconstructed from the mode spectrum by Chandler & Lama method (solid line), "Energy to recoils" curve (dashed line) computed by TRIM, experimental values of the effective indices (squares).

## 2.2 Thermal stability of the amorphized regions

A necessary condition for making RI_Eng a viable fabrication technology for constructing electrooptical circuits is that the structures formed by the implantation process are thermally stable. It was found that the thermal stability can be attained by annealing the structures at elevated temperatures.

A study of the effect of the annealing process was conducted in the slab WGs described above, i.e. the WGs generated by the implantation of $He^+$ ions at 2.3 MeV which created an amorphized layer ≈5μm below the surface of the substrate with a thickness of ≈0.5 μm and peak reduction of the RI of 5%.

The WGs were annealed isothermally for exponentially growing periods of time in the tube furnace at $\approx 351^0$ and $\approx 456^0$C respectively. Following each annealing step the residual RI drop Δn was reconstructed from the dark mode spectrum measured using a prism coupler setup operating at wavelength of λ=1.3 μm. The results of this process are shown on Figure 3. The recovery of the RI drop was found to converge in time asymptotically to a constant. Furthermore it was shown that the constant approaches zero as the annealing temperature is increased. This behavior points to the fact that following annealing for several hours the sample is expected to be thermally stable for any temperature lower than the annealing temperature. Reliability check which included storage of the sample for a week at elevated temperature of $150^0$C has shown complete thermal stability of the annealed samples.

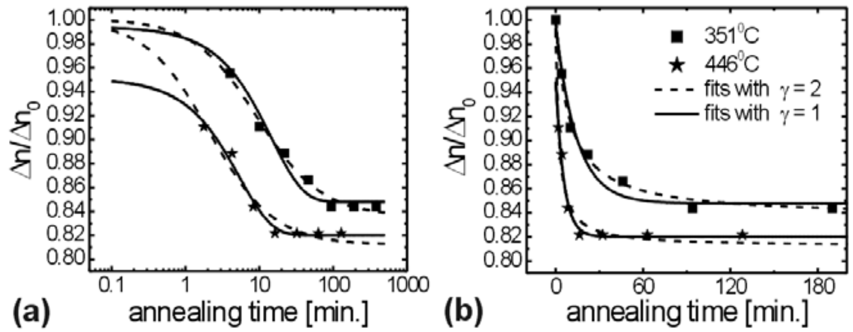

Figure 3. Isothermal annealing curves of annealed WGs with fits for two cases of the order of the chemical reaction γ describing the diffusion of Frenkel defects composing the implanted amorphous layer (a) on logarithmic time scale and (b) on linear time scale.

### 2.3 Design methodology of the implantation protocol

Effective utilization of the implantation process as a generic method for integrating electrooptic and photonic devices in a waveguided architecture necessitates the development of computational tools that will yield advanced knowledge of the RI profile resulting from the implantation process. It was shown that the TRIM simulation program gives a good estimate of the geometrical profile of the RI produced in the substrate given the implantation parameters and the density of the substrate. However, in order to assign absolute value of the RI to the profile, it was necessary to perform direct measurements of the optical modes that propagate in the produced WG and use the obtained data to fit the simulated profile to absolute values of the RI.

A general method for predicting the change in the RI generated in an implantation process was derived from the simple radiation damage model described in [9]. In this model the peak value of the RI change in the amorphous layer Δn can be expressed in terms of a universal implantation parameter P independent of the type of the implanted ion, given by $P=(0.4D/\rho)\cdot(dE_n/dx)$, where $dE_n/dx$ can be calculated by TRIM. In terms of P, Δn is given by

$$\Delta n = \Delta n_{\max}\left[1-\exp\left(-\frac{P}{E_D}\right)\right] \tag{3}$$

$\Delta n_{max}$ is the maximal achievable RI change and the $E_D$ is the average energy needed to displace an atom in the lattice from its original site. It was observed that implantation of very high doses of ions causes the formation of a mosaic pattern of macroscopic defects due to stress along the crystallographic axis. These cause significant changes in the RI of the amorphous layer, in addition to those produced by the Frenkel defects.

As an example consider the implantation of $C^{+4}$ and $O^{+5}$ ions in a KLTN substrate. $\Delta n_{max}$ and $E_D$ were derived by fitting equation (3) to the experimental data summarized in Table 1. Results of the fitting process are presented graphically in Figure 4. For each experimental point, $dE_n/dx$ was computed separately by TRIM so that only two free parameters were obtained by the fitting process. For this particular case it was found that $E_D$=5.7±0.3 eV, and $\Delta n_{max}/n_o$=11.4±0.3%. The RI of the unperturbed KLTN substrate used in the experiments, was measured to be $n_o$=2.194. The fitting of equation (3) to the experimental data presented in Figure 4 can be used to predict the drop in the RI caused by the implantation of any ion in a KLTN substrate provided the dosage is known, and $dE_n/dx$ was computed by TRIM for the implanted ion.

It should also be noted that the formation energies of the intrinsic vacancies of Nb in $KNbO_3$ [10], of Ta in $KTaO_3$ [11] and of O in both materials [10,11] are significantly higher than the displacement energy resulting from the fit of (3) to the experimental data (Figure 4). Thus it can be assumed that the Frenkel defects mainly of K ions influence the buildup of Δn. This is substantiated further by estimating the effective formation energy of the K vacancies in the KLTN samples. The formation energies of the K vacancies as given by Donnerberg [10,11] are 4.1eV for $KNbO_3$ and 6.7eV for $KTaO_3$. We used KLTN samples in which the Ta:Nb ratio is 0.68:0.32. Under the assumption that the formation energy of the K vacancy in our samples can be estimated from a weighted average according to the Ta:Nb ratio, the effective value for the formation energy of the K vacancies is given by 5.8eV.

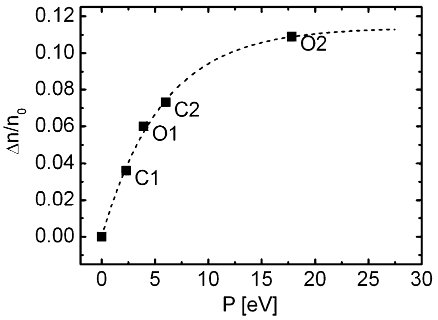

Figure 4. The fitting of to the experimental data of the semiemprical formula describing the relative change in the RI [$\Delta n/n_o$] vs. the unified implantation parameter P and the nuclear stopping deposition energy $E_D$. The squares are the experimental points used to derive the curve.

Table 1. Implantation conditions and resulting WG parameters.

| Sample name | Implanted ion | Ion Energy [MeV] | Average ion current [nA] | Dosage [$10^{14}$ ion/cm$^2$] | Amorphous layer depth [μm] | Δn [%$n_o$ of bulk] |
|---|---|---|---|---|---|---|
| C1 | $^{12}C^{+4}$ | 30 | 30 | 6.3 | 17.7±0.1 | 3.6 |
| C2 | $^{12}C^{+4}$ | 30 | 150 | 16.4 | 17.7±0.1 | 7.3 |
| O1 | $^{16}O^{+5}$ | 40 | 55 | 5.9 | 16.3±0.3 | 5.9 |
| O2 | $^{16}O^{+5}$ | 30 | 120 | 27.0 | 11.8±0.1 | 10.9 |

In summary, augmenting the basic implantation process with the ability to predict the change in the RI in the implanted regions paves the way for a generic method for constructing complex electrooptic circuits. The combination of TRIM with the method for computing the RI in the implanted regions provides a comprehensive programming tool for designing the fabrication process of these structures.

## 3. THE TOOLBOX OF REFRACTIVE INDEX ENGINEERING

Electrooptical circuits constructed by RI_Eng are in essence an ensemble of 3D structures with reduced RI assembled together in the KLTN substrate. Hence, the basic operation of the RI engineer is to sculpt a 3D structure with predesigned spatial distribution of the RI.

The sculpting of these structures is done by performing a series of implantation sessions each of which constitute a combination of longitudinal and lateral patterning of the RI in preselected region of the substrate.

An implantation session consists of three elements:

1. Longitudinal patterning: Determining the depth at which the amorphization occurs by controlling the initial energy of the implanted ions.
2. Lateral patterning: Determining the lateral distribution of the amorphization by restricting the areas at which the implanted ions penetrate the substrate.
3. RI modulation Setting the required change in the RI induced in the amorphized regions by controlling the dosage of the implantation using the semi-empirical formula described above.

### 3.1 Longitudinal Patterning

As pointed out above, the depth at which the amorphization occurs is determined by the initial energy of the implanted ions. The initial energy for creating the amorphized layer at the required depth, for a given species of implanted ions and a given substrate is provided by TRIM. The level of change in the RI in the amorphized layer can be determined by setting the dosage of the implantation session derived by applying the semi-empirical formula [9].

A demonstration of longitudinal patterning is the submerged slab WG. The WG was constructed in a KLTN substrate with $T_c$=11.2 °C. The core of the WG is sandwiched between two amorphized layers positioned well within the depth of the substrate and act as the top and bottom cladding of the WG. The amorphized layers were fabricated by two successive implantation sessions. The implanted ions were $C^{+5}$. The first session was done by implanting a dosage of $0.47\cdot 10^{15}$ ions/cm$^2$ at 30 MeV, and the second session was done by implanting a dosage of $0.9\cdot 10^{15}$ ions/cm$^2$ at 40 MeV. This created two amorphous layers that were formed at different depths which manifested an RI profile that forms three slab WGs: WG A immediately beneath the surface of the substrate cladded between the air and the first amorphous layer, WG B submerged in the depth of the substrate cladded between the two amorphous layers, and WG C cladded between the air and the second amorphous layer. The predicted geometry of the three WGs as predicted by the TRIM simulation and the semi-empirical formula is presented in Figure 5. The first amorphous layer is formed 17.7 μm below the surface of the substrate and has a width of 0.6 μm (defined as FWHM), the second amorphous layer was formed 26.1 μm below the surface of the substrate with a width of 0.65 μm. The two layers form the cladding for a buried WG with a width of 8.4 μm. The peak of the relative decrease of the RI in the amorphous layers that was formed by the implantation was found to be 2.8% for the first amorphous layer and 4.8% for the second layer.

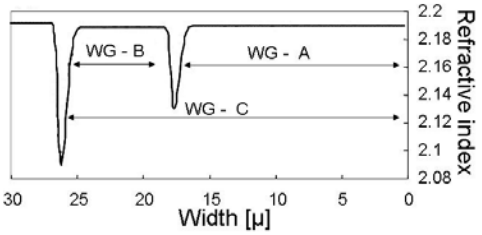

Figure 5. RI profile of KLTN sample after carbon ions implantations at 30MeV and 40 MeV

Direct observation of the light-wave as it propagates through the WGs was obtained by illuminating the input plane of the WGs while observing the light as it emerges from the output plane. In Figure 6a, a section of the output plane of the sample is shown while the input plane was illuminated by the white light source of the microscope. The amorphous layers that were formed by the implantation are clearly seen at 17.7 μm and 26.1 μm below the surface of the crystal. It should be mentioned that the defects that appear near the surface of the sample are due to edge crumbling at the front surface that occurred during the polishing of the crystal, and are not an outcome of the implantation. In Figure 6b the same section of the output plane of the sample is shown while light was coupled directly into WG B that was formed between the two amorphous layers. The light source was a diode laser operating $\lambda = 670nm$ that was focused by a tapered lensed fiber into a spot of less than 5 μm in diameter. It can be seen that the light propagating in the sample is well confined between the two amorphous layers that function as the cladding of the submerged WG B. More details of this experiment are given in Ref [12].

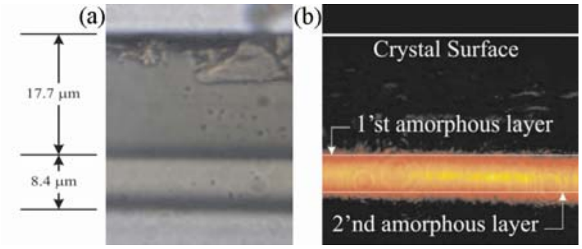

Figure 6. View of the output plane of the submerged WG, (a) while the input plane was illuminated by the white light source of the microscope; (b) while light at $\lambda = 670nm$ was coupled directly into WG B.

### 3.2 Lateral patterning

The lateral patterning is done by restricting the penetration areas of the implanted ions into the substrate to predefined locations. This is accomplished by applying the concept of the *stopping mask* that governs the lateral-spatial distribution of the implantation. The stopping mask is constructed of a metallic film with varying thickness that determines the penetration depth of the implanted ions at each location on the surface of the KLTN substrate. Thus, the distribution of the Frenkel defects which are created during the implantation replicates the contour of the topography of the stopping mask. The average depth of the implanted layer is set by adjusting the initial energy of the implanted ions [12]. Hence the combination of a series of implantation sessions at different initial energies through a respective set of stopping masks enables the construction of complex multi level 3D structures with minute features within the depth of the substrate. Designing the stopping mask, selecting the implantation energy and choosing the right dosage, for a given RI structure, must take into account the character of the specific implantation parameters and the composition of the substrate. This is done by combining the TRIM simulation with the semi-empirical formula [9]. For example: TRIM simulations predict that $He^+$ ions at 2.3 MeV reaches a depth of 5μm when implanted into a KLTN substrate, and a depth of 3.3μm when implanted in gold, *i.e.* the Gold-KLTN implantation stopping ratio is 0.66. Given the geometrical features of the structures to be constructed, this ratio can be used to derive the thickness distribution of the gold stopping mask. It can also be used to derive the slopes in the gold mask that will be reproduced in the amorphous structure within the KLTN substrate. The steepness of the slopes will increase in correspondence with the Gold-KLTN stopping ratio. In addition as predicted by TRIM and shown in Figure 7 for $He^+$ ions with implantation energies of 1MeV-2.5MeV the width of the amorphous layer, is 0.45μm-0.48μm. TRIM simulations also predict that the corresponding lateral range of the implanted ions is 0.23μm-0.32μm. (Note that this provides in addition the minimal RI feature size that can be created by the selective ion implantation method).

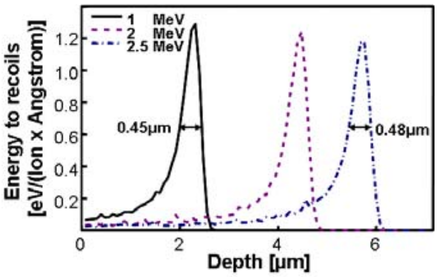

Figure 7. TRIM simulations of the implantation process for different energies of implantation. For a given dosage the "energy to recoil" axes expresses the level of amorphization which induces the change in the RI.

A demonstration of lateral patterning by applying the concept of the stopping mask is the channel WG constructed by one implantation session of He$^+$ ions. The core of the channel WG was submerged beneath the substrate surface and surrounded by a cladding with trapezoidal profile. Fabricating the WG by a single session of ion implantations, i.e. implantation by one ion species at a single energy through a single stopping mask necessitated the construction of a gold mask with a trapezoidal groove. The designed channel WG and the designed stopping mask are illustrated in Figure 8a and 8b respectively.

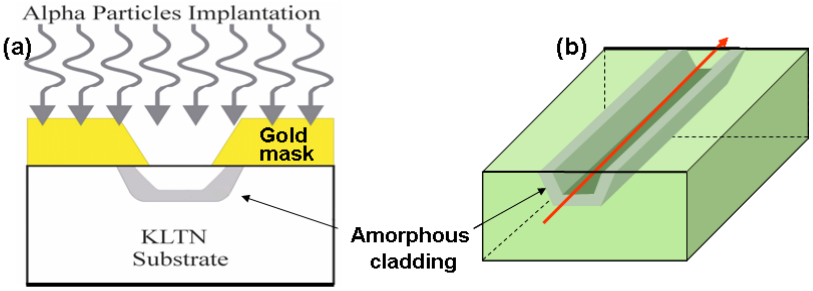

Figure 8. The 1D channel WG and the gold stopping mask used for its fabrication: (a) The profile of the designed gold mask; (b) A schematic illustration of the designed channel WG.

The Gold mask was constructed on a KLTN substrate with $T_c$=12.6°C. The mask was formed as follows: (i) a gold layer with a thickness of 0.2 µm was deposited onto the KLTN crystalline substrate; (ii) a 6µm wide slit was opened in the deposited gold layer by lithography and etching; (iii) 2 µm thick gold film was grown on top of the deposited layer using the electroplating technique. By nature of the gold electroplating process the slit was gradually closed forming sloped gold walls. The steepness of the gold walls in the test sample was found to be 51˚±3˚. It was estimated that due to the Gold-KLTN stopping ratio, these will be transformed to amorphous KLTN walls with steepness of 62˚±3˚.

The KLTN substrate plus the gold mask were bombarded with a beam of He$^+$ ions with energy of 1.65MeV. A dosage of $1.78 \cdot 10^{16}$ ions/cm$^2$ was implanted into the sample. This yielded a trapezoid like amorphous structure with a thickness of 0.45 µm. Inserting the implantation properties into the semi-empirical formula, and taking into account the geometry of the implantation, indicates that the maximum RI reduction in the trapezoidal cladding layer is 10%±0.6% and 7%±0.6% in the base and the sides of the trapezoid respectively. After the ion implantation the Gold mask was removed by wet etching and a plate of optical grade silica was attached to the surface of the sample. The sides of the sample were then polished to optical quality.

A reflection microscope image of the surface of the implanted sample is presented in Figure 9a. The image shows the amorphous region viewed from above the trapezoidal profile along the channel WG. The width of the upper base of the channel WG is 2.9±0.2µm, measured between the inner sides of the trapezoid. Figure 9b shows a transmission microscope picture of a cut view of the channel WG, it indicates that the height of the channel WG measured between the upper and the lower bases of the trapezoid is 3.6±0.2µm, which is in agreement with the TRIM prediction for implantation energy of 1.65MeV. The lower base of the trapezoid is 1.1±0.2µm. The entire sample was back illuminated by the white light source of the microscope. Simultaneously a laser beam at 532 nm with a beam diameter of approximately 2 µm was focused onto the core of the WG at the input plane. Figure 9c is a direct observation of the light-wave that propagates through the 3.2mm long channel WG as it emerges from its output. It can be seen that the light propagating in the sample is well confined within the core of the channel WG. More details of this sample are given in Ref. [13].

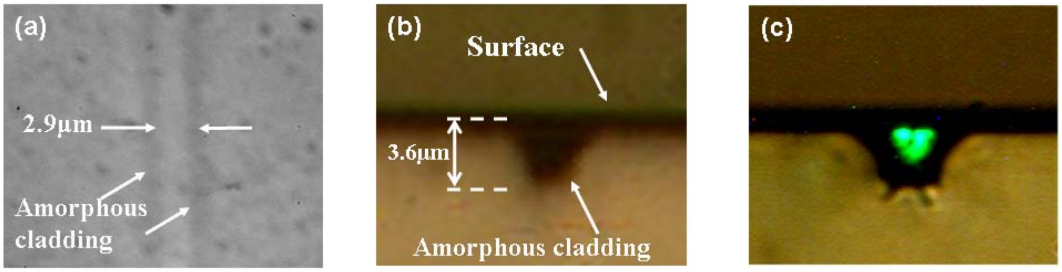

Figure 9. Microscope images of the channel WG that was fabricated using the RI_Eng method, (a) top view; (b) side view; (c) The spatial distribution of light intensity at the output of the channel WG at λ=532nm as it emerges from the channel WG output;

### 3.3 Construction of electrically conducting structures

Constructing EO devices within the depth of the KLTN substrate necessitates being able to place the driving electrodes of the devices within the depth of the substrate as well. Hence it is necessary to be able to construct 3D structures that are submerged within the substrate and are electrically conducting. The technique for constructing electrically conducting structures is based on the implantation of protons in the KLTN substrate. It was found the implantation a high concentration of protons in the KLTN substrate creates a black amorphized layer with reduced RI that is in addition both electrically conducting and photoconducting [14].

These phenomena are demonstrated in the following experiments: Two KLTN samples were bombarded by a proton beam, sample S1 with 1.6MeV and a dosage of $1.16 \cdot 10^{17}$ ions/cm$^2$, and sample S2 with 0.6MeV and a dosage of $0.8 \cdot 10^{17}$. The resistance of the conductive layer in sample S1 was found to be 2.1kΩ at room temperature which translated to conductivity of 312 (m·Ω)$^{-1}$. Measurement of the conductivity in the temperature range 298K – 333K manifested an Arrhenious behavior $\sigma = A\exp\left(-Ea/KT\right)$ with activation energy $Ea = 0.094eV$. The electric conductivity profile in the amorphized layer in sample S2 was measured by an AFM system by the set up illustrated schematically in Figure 10a. The conductivity as a function of the depth in the KLTN substrate is shown in Figure 10b. A comparison to a TRIM simulation of the protons distribution profile also in Figure 10b suggests that the conductivity is caused by the protons.

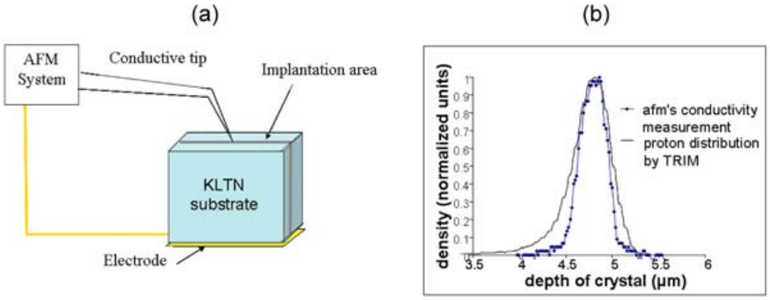

Figure 10. Conductivity measurement: (a) The AFM set up. On one side of the implantation area a permanent electrode was deposited, and on the other a conductive tip. (b) A comparison between the AFM's conductivity profile and the protons distribution profile by TRIM of sample S2.

The optical absorption of sample s2 was measured by a spectrophotometer (in the wavelengths range 400nm-2100nm), and by FTIR (in the wavelengths range 1.92μm-22μm). The results are presented in Figure 11. The maximum of the absorption was found to be at $\lambda = 1.62$μm (equivalent to $h\nu = 0.77$ev). In order to find out if the source of the optical absorption of the layer is related to excitation of charge carriers sample S1 was illuminated with photodiode of wavelength 1.55μm (0.8eV) while running current measurement on the sample at room temperature. As can be seen in Figure 12, while the sample is illuminated (110-190 seconds) there is a significant addition to the current that depends linearly on the light intensity and can be interpreted as photoconductivity.

The proton implantation opens the way for constructing the driving electrodes of the EO devices within the depth of the substrate. This enables to construct complex circuits in which many EO devices are integrated together. Furthermore, the conducting structures open the way for a new class of 3D photonic devices in which conducting and insulating components are integrated together.

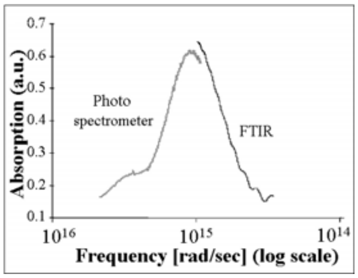

Figure 11. The absorbance profile of sample S2 that measured by photo spectrometer and FTIR.

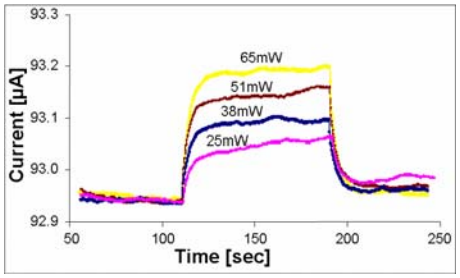

Figure 12. The current addition caused by illumination of sample S1 by 1.55µm photodiode between the seconds 110-190.

### 3.4 Selective Etching:

Selective etching is a technique for creating trenches, cavities, and tunnels both on the surface and within the depth of the KLTN substrate. The technique exploits the fact that the solubility of the amorphized regions created by the implantation is significantly greater than that of the KLTN crystalline material. This concept was first demonstarted by etching the amorphphous layer formed by the implantation of $He^+$ ions at 2.3 MeVs. The formed amorphous layer was 0.5 µm wide (FWHM), centered approximately 5 µm below the surface of KLTN substrate. Initial result of etching by a 50/50 mixture of HF and $HNO_3$ for 20 minutes at 35°C is shown in Figure 13. It can be seen that the etched region is restricted to the amorphized layer that was created by the implantation. Note that Figure 13 does not reflect the full depth of the etching as it is limited by the ability of the AFM tip to penetrate the trench.

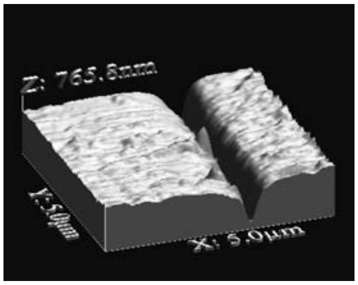

Figure 13. An AFM image of the amorphous layer after etching for 20 min in a 50/50 mixture of $HNO_3$ and HF at 35°C

The etching of a deep trench is shown in Figure 14. The implanted region was a 300 µm strip that was created by the implantation of $He^+$ particles at 2.0 MeV. The depth of the strip was 4.0 µm below the surface of the crystal, and approximately 1.5 mm away from each side of the substrate. In Figure 14 one side of the substrate was polished in order to expose the full depth of the etch trench. As can be seen it was possible to etch a narrow trench well into the depth of the substrate. Note that the width of the trench is maintained constant (although slightly wider than the width of the implanted layer). The spear-like section in the deepest part of the trench is a result of the the distribution profile of the

Frenkel defects created by the implantation. It is expected that a sophisticated implantation protocol which consists of several implantation sessions at different energies and different dosages will refine the control of the shape of the formed trench [15].

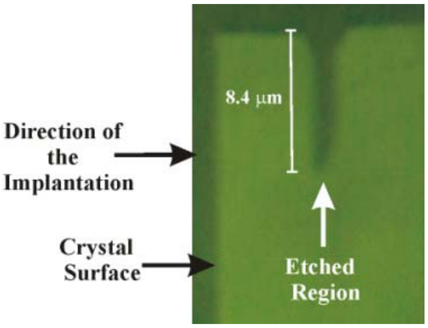

Figure 14. Optical image of an 8.4 μm deep trench etched within the volume of the substrate.

The selective etching opens the way for a multitude of possibilities. First, it enables the construction of waveguiding structures that are cladded by air, so that the contrast between the core and cladding is very large. Thus, small curvatures can be implemented while maintaining small bending losses. Second, it provides a technique for constructing nanophotonic devices with subwavelength features and very large RI contrast. Moreover, the etched spaces created by the selective etching process can be filled by different materials such as nonlinear materials which give tremendous flexibility in the hands of the circuit designer. Third, selective etching can be the basic tool for constructing microfluidic devices that are integrated as part of the EO circuits. And fourth, selective etching can be the basic tool for constructing micro electromechanical systems (MEMS), and Nanoelectromechanical systems (NEMS) on KLTN substrates in which the actuator, the optical device and the electrical device are fabricated in the same material system.

## 4. CHANNEL WAVEGUIDE ARRAY CONSTRUCTED BY A COMPLETE PROCESS FLOW

In order to demonstrate the potential of RI_Eng, a channel array WG was constructed by a complete process flow in which both lateral and longitudinal techniques were applied. In general, WG arrays are used for optical switching, power management and wavelength demultiplexing in optical fiber communication networks. The device described here is the basic WG array structure consisting of an array of identical channel WGs. Beyond providing a full demonstration of a device fabricated by a multistage process in which both lateral patterning and longitudinal patterning were applied, it verified that the electrooptical devices with amorphous regions embedded in their structure maintain their electrooptic activity. In particular, in the channel array WG it was shown that the coupling between adjacent channels separated by an amorphized wall can be controlled by an electric field. Thus the channel array WG demonstrated that the method of RI_Eng by ion implantations can indeed become a generic method for constructing electrooptical integrated circuits.

Consider Figure 15 depicting a schematic illustration of the WG array. The array is designed and constructed so that there is a significant crosstalk between the adjacent channels. Thus if light is coupled to the central channel in the input plane, it couples to neighboring channels during its propagation, and emerges in the output plane in the form of a supermode. The intensity distribution at the output plane is expected to be a function of the interchannel coupling constant. The latter depends on the core-cladding RI contrast, which can be tuned by applying an electric field across the device. Hence, the application of the field across the device is expected to cause observable changes in the supermode intensity distribution.

The WG array was constructed in a KLTN crystalline substrate. The array is cladded from the top by the air above the surface of the KLTN substrate, and from the bottom by a layer of partially amorphized material with reduced RI. The core of each channel WG in the array is the crystalline KLTN material of the substrate. The sidewall claddings between the WGs are constructed of partially amorphized material with reduced RI.

The WG array was fabricated by performing a series of implantations of $He^+$ ions at different energies and dosages through a comb-like stopping mask. The stopping mask used was a square grating constructed of alternating stripes of gold and SU8 polymer. The mask was 2.9 μm thick. The grating period was 3.5 μm. The gold/SU8 widths ratio in each period was ≈5/2. The process flow for constructing the mask is presented in Figure (16a) to (16e). First, a 20 nm Cr layer and a 200 nm Au layer were evaporated onto the KLTN substrate (Fig. 16b). Then a 2.7 μm thick layer of SU8 was spin coated on top of the gold layer (Fig. 16c). Using conventional optical lithography methods, a periodic grating of stripes that were 2.5 μm wide was opened in the SU8 layer exposing the 200 nm gold layer, and leaving 1 μm wide SU8 stripes between the gold stripes (Fig. 16d). Finally, using electroplating techniques for which the thin gold layer served as seed electrode, the empty stripes between the SU8 stripes were filled with gold (Fig. 16e).

The process flow for constructing the channel WG array consisted of a multistage process which consisted both lateral patterning and longitudinal patterning as described above. Specifically, the process flow for constructing the WG array consisted of a series of three implantation sessions: (i) a dosage of $3.0\text{x}10^{15}$ $He^+$ ions/cm$^2$ at the energy of 1.6 MeV implanted through the mask; (ii) a dosage of $3.2\text{x}10^{15}$ $He^+$ ions/cm$^2$ at 1.2 MeV implanted through the mask; and (iii) a dosage of $11.1\text{x}10^{15}$ $He^+$ ions/cm$^2$ at energy of 1.8MeV implanted directly into the KLTN substrate after the mask was removed. The process flow is described schematically in Figures 16f, 16g, and 16h.

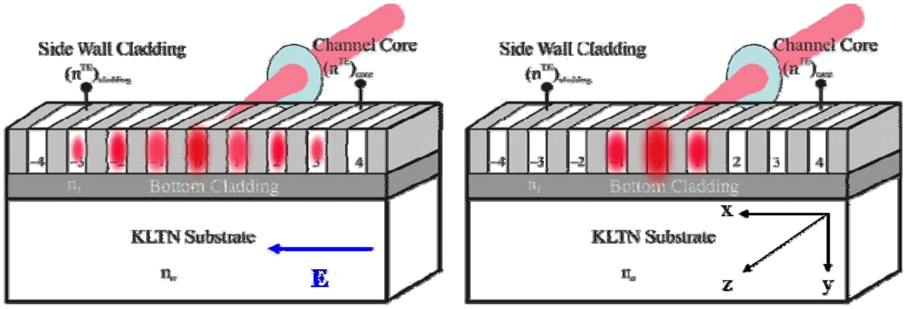

Figure 15. Schematic description of the channel array

The thickness of the gold layer was designed to prevent the implanted ions in implantations sessions (i) and (ii) from penetrating the KLTN substrate. Hence, the material beneath the gold covered sections of the grating was not exposed to the implantations, and remained crystalline KLTN. The stopping power of the 2.7 μm thick SU8 + 0.2 μm thick Au sections is significantly smaller than that of the Au sections of the thickness of 2.9 μm , since the specific density of SU8 is lower than that of the Au. (The specific densities fed into TRIM were $\rho_{SU8}$=1.15 g/cm$^3$, $\rho_{Au}$=19.31 g/cm$^3$, $\rho_{KLTN}$=6.12 g/cm$^3$). Hence, implantations sessions (i) and (ii) of the implantations protocol created in the areas beneath the SU-8 covered sections of the grating an amorphized layer with reduced RI. The implantation session (iii) that was performed after the stopping mask was removed created a uniform amorphized layer beneath the grating that will act as the bottom cladding for the entire WG array.

The expected core-cladding RI distribution along the x axis for the structure fabricated by this process flow was computed by the procedure described in reference [16] and is presented therein.

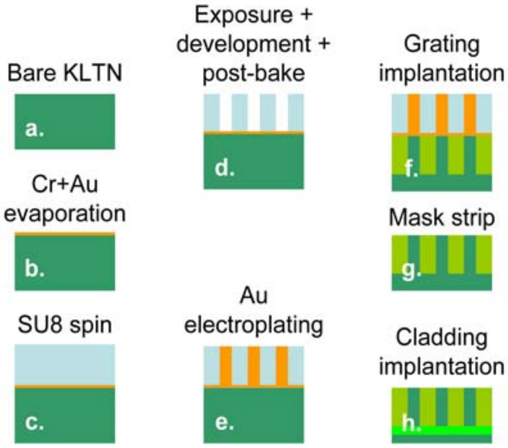

Figure 16. Process flow for the construction of the channel array

The WG array was fabricated in a KLTN substrate with composition given by $K_{0.997}Li_{0.003}Ta_{0.621}Nb_{0.379}O_3$ yielding a phase transition at $T_c$=15.5 °C, and dimensions of 10x10x1.5 mm$^3$. The RI at room temperature at $\lambda$=633nm was $n_o$=2.2677. One of the substrate xz 10x10 mm$^2$ faces was polished to optical grade quality and subjected to the implantations protocols given above. After completing the implantations, the crystal was cut to a 5.3 mm long sample along the z axis. The xy faces of the crystal were polished to optical grade, and the yz faces were deposited with gold electrodes.

A preliminary study of the device was done by direct observation through an optical microscope. The WG array was illuminated by focusing a white light source at the input plane through an inverse microscope. The image of the intensity at the output plane is shown in Figures 17(a) and 17(b). As can be seen the light that enters the WG array couples through the side claddings into the neighboring channels as it propagates along the channels, yet staying confined to a small number (~20) of channels in the output.

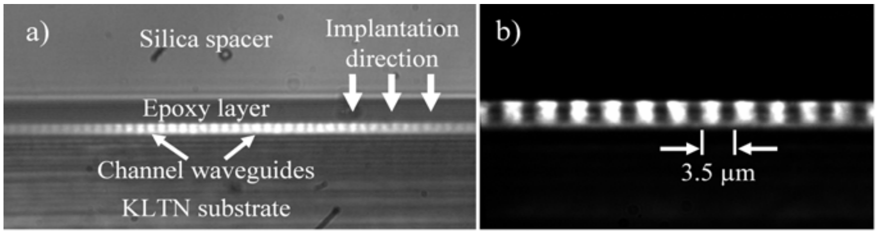

Figure 17. (a) View of the front end of the channel WG array illuminated from the back by a white light source. Silica spacers were attached to the top of the array at the front and back ends. The spacers were a 150 μm thick and 1.5 mm wide, and were attached to the substrate by a ~10 μm thick transparent epoxy layer. (b) Enlarged image of the front end central section of the array with inverse log scale of the intensity.

Further detailed quantitative study of light propagation in the WG array was done by measurements of the near field at the output plane that was generated by a monochromatic beam at $\lambda=636\pm2$ nm focused into the central channel in the input plane. The light emanating from the output plane was collected by a microscope with a x100 objective, and was imaged onto the detector array of a CCD camera.

The coupling between the channels was modulated by applying an electric field along the x-axis. The device temperature during the experiment was maintained at T=19°C (3.5°C above $T_c$). The intensity of the near field distribution at the output plane taken at different levels of the applied field in the range between zero and 4 kV/cm are shown in Figure 18. It can be seen that the coupling is enhanced strongly as the applied electric field is increased. A qualitative analysis of the results shown below requires estimating the effect of the applied field on the coupling. If the electric field is applied across the width of the crystal then for the TE modes $g_{eff}=g_{11}=0.16$ m$^4$/C$^2$, whereas for the TM mode $g_{eff}=g_{12}=-0.02$ m$^4$/C$^2$. Note also that $g_{11}>0$ whereas $g_{12}<0$, so that applying the field will increase the coupling for the TE mode, and decrease the coupling for the TM mode. Thus, applying the field is expected to cause the TE component of the light at the output plane to be more widely distributed across the array, whereas it is expected to cause the TM component to become more confined to the central channels.

In our case it was observed that the coupling between neighboring channels increases as the field increases. According to the discussion above this implies that the light propagating in the array is dominated by TE modes for which $g_{eff}=g_{11}$ so that $\Delta n<0$ in the electrooptic core region. We are thus assuming that the light propagating in the WG array is a superposition of only TE modes. Limiting ourselves to two modes, the output intensity is given by

$$I(x,z)=\sum_{l=1}^{2}\left(A_l\left|\sum_{m=-10}^{10}(-i)^m J_m(2\mathrm{K}_l z)\exp\left(-\frac{1}{2}\alpha z\right)\exp\left(-\frac{(x-md)^2}{\sigma^2}\right)\right|\right)^2 . \quad (4)$$

Here, l is the index of the array in which the inter-channel coupling constant $K_l$ of the basic $(E^x)_{11}$ mode is equal to the inter-channel coupling constant of true respective mode in the actual WG array, $A_l$ is the relative amplitude of the mode propagating in the l'th array, and $\sigma=2.04$ μm is the width along the x direction of the $(E^x)_{11}$ mode, propagating in a single channel. The width of the mode σ was estimated in a slab WG approximation for which $(n_{TE})_{core}=2.2517$ and $(n_{TE})_{cladding}=2.2305$ as computed above. α is the attenuation constant originating from the absorption and scattering for a mode propagating in the z direction. The calculation in (4) is restricted to the 10 channels on both sides of the central channel, because for the relevant wavelength the intensity is assumed to be confined mostly to the ~20 central channels, as we observed on Figure 17(a). Note that it is assumed in (4) that inter-modal coupling does not occur, so that the overall power of each of the two propagating modes remains constant as they propagate through the channel. (detailed discussion of the arguments leading to (4) are given in reference [16].

Curves of the intensity across the array for the set of images of the output plane are shown in Figure 18. Also shown in Figure 18 is the intensity across the x axis sampled from the images. We reconstruct the effective RI contrast between the core and the inter-channel cladding for each level of the applied electric field as the product of the fitting procedure of (4) to the experimental intensity distribution in which the modal coupling constants are the free parameters. It can be seen that (4) provides very good fitting to the experimental data. It should be noted that indeed the output intensity can be approximated by the superposition of two TE modes with constant ratio between their amplitudes (i.e. independent of the applied field). This substantiates the assumptions adopted in (4) for approximating the output intensity by superimposing a set of two arrays. The effective RI contrast between the core and the side cladding of the channels in the array for different levels of the applied field for the basic $(E^x)_{11}$ modes in the two superimposed WG arrays which constitute the device are presented in Figure 19. We assume that the mode for which the contrast is higher is the true basic $(E^x)_{11}$ mode in WG array. Note in particular that the effective RI contrast between the channel core and side cladding for the basic mode was changed by 0.4 % when the applied field was varied from 0 to 4 kV/cm. In bulk KLTN the maximal electrooptically induced change in the birefringence is 0.5 %. This indicates that the electrooptic effect is not inhibited by the implantations, contrary to what was reported for WG devices fabricated in other oxygen perovskites such as $LiNbO_3$ [17].

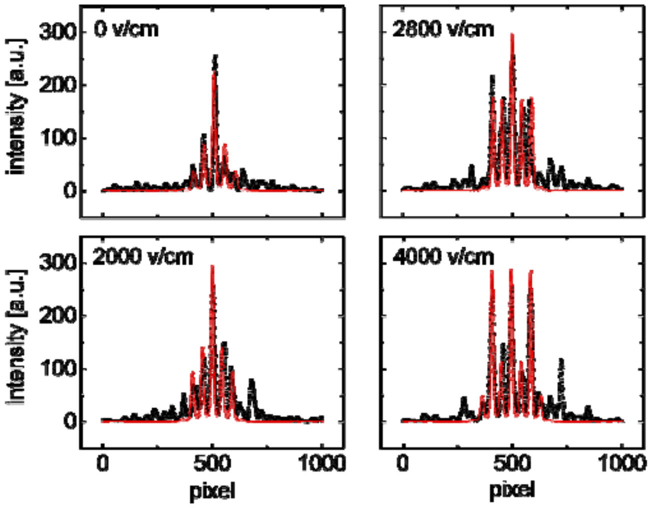

Figure 18. The measured and the processed intensity distributions in the output plane of the device at different voltages (solid black + symbol) and the respective fits of (4) (solid red). The intensity on the snapshots is inverse-log scaled by the image processing software of the CCD camera; the fits of (4) were converted to inverse-log scale respectively.

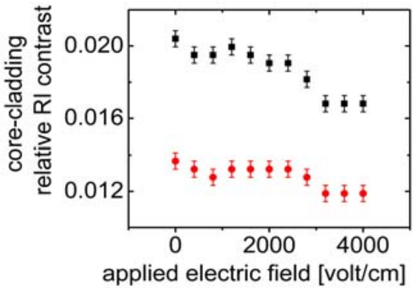

Figure 19. The RI contrast between the core and the inter-channel cladding in a single channel of the array for 2 dominant modes.

## 5. SUMMARY AND CONCLUSIONS

It was shown hitherto that RI_Eng can become a generic technique for constructing 3D structures within the volume of optical perovskite crystals. RI_Eng was demonstrated above in KLTN substrates; however, the device physics of RI_Eng is not limited to a specific material system such as the KLTN crystal. KLTN was chosen as it has several generic advantages: First KLTN can be grown by metal-organic chemical vapor deposition on a wide range of substrates including silicon, silicon oxide and alumina oxide [2]. Second, at the paraelectric phase KLTN has a very strong electrooptic effect. Third, KLTN can be the substrate for electrooptical devices that are operated in the near infrared and visible spectral ranges while remaining immune to space-charge driven optical damage. In addition, KLTN has several advantages as the substrate for constructing electrooptical circuits by the RI_Eng technique: The implantation process enables the construction 3D structures with subwavelength features that are thermally stable in which the RI is reduced by ≈10% with very little deterioration in the optical quality. It is possible to construct regions that are electrically conductive within the depth of the KLTN substrate. And, it should also be possible (using the concept of selective etching) to develop a microfluidic technology in KLTN substrate. As such, RI_Eng combined with the electrooptical properties of KLTN has the necessary elements to become a fabrication technology for electrooptical circuits that adopts the three principles that are at the basis of very large scale integration (VLSI) of microelectronic circuits: (i) Implementing all the different devices in the circuit by be the same device physics; (ii) Providing Computer Aided Design tools which render the device physics transparent to the designer; and (iii) Fabricating the entire circuit as one integrated unit using the same fabrication technology rather than fabricating each component separately, and assembling the circuit using a "pick and place" technique.

In conclusion, RI_Eng has the potential to become a generic methodology for constructing complex electrooptic circuits in which a multitude of optical components, electrooptic devices and nanophotonic structures are integrated together and function in unison.

## AKNOWLEDGMENTS

We acknowledge the support of the Eshkol Fellowships Foundation, Grants No. 3-4341 and 3-6435, of the Israeli Ministry of Science.

## REFERENCES

[1] R. Hofmeister, S. Yagi, A. Yariv, and A. J. Agranat, "Growth and Characterization of KLTN:Cu,V Photorefractive Crystals", J. Cryst. Growth 131, 486-494 (1993).

[2] M. Sasaura, K. Fujiura, K. Enbutsu, T. Imai, S. Yagi, T. Kurihara, M. Abe, S. Toyoda, and E. Kubota, "Optical waveguide and method of manufacture", US Patent Application 0072550 (2003).

[3] D. Kip, "Photorefractive waveguides in oxide crystals: fabrication, properties, and applications" Appl. Phys. B, Laser Optics 67, 131-150 (1998).

[4] G.H. Kinchin and R.S. Pease, "The displacement of atoms in solids by radiation", Rep. Prog. Phys. 18, 1-51 (1955).

[5] J. Lindhard, M. Scharff, H.E. Schiott, "Range concepts and heavy ion ranges. (Notes on atomic collisions, II.)", Mat. Fys. Medd. Dan. Vidensk. Selsk. 33, 1-42 (1963).

[6] J. F. Ziegler, J. P. Biersack, and U. Littmark, "The Stopping and Range of Ions in Solids" Pergamon, New York, (1985). http://srim.org/

[7] A. Gumennik, A. J. Agranat, I. Shachar, and M. Hass, "Thermal stability of a slab waveguide implemented by alpha particles implantation in potassium lithium tantalate niobate," Appl. Phys. Lett. 87, 251917-1-3 (2005).

[8] P. J. Chandler, and F. L. Lama, "A New Approach to the Determination of Planar Wave-Guide Profiles by Means of a Nonstationary Mode Index Calculation," Optica Acta 33, 127-143 (1986).

[9] A. Gumennik, H. Ilan, R. Fathei, A. Israel, A. J. Agranat, I. Shachar and M. Hass, "Design methodology of refractive index engineering by implantation of high-energy particles in electro-optic materials", Appl. Opt. 46, 4132-4137 (2007).

[10] M. Exner, H. Donnerberg, C. R. A. Catlow, and O. F. Schirmer, "Computer-Simulation of Defects in $KTaO_3$," Phys. Rev. B 52, 3930-3940 (1995).

[11] H. Donnerberg, "*Atomic Simulation of Electrooptic and Magnetooptic Oxide Materials*" Springer-Verlag, Berlin, (1999).

[12] H. Ilan, A. Gumennik, R. Fathei, A. J. Agranat, I. Shachar, and M. Hass,"Submerged waveguide constructed by the implantation of $^{12}C$ ions in electrooptic crystals". Appl. Phys. Lett 89, 241130 (2006).

[13] H. Ilan, A. Gumennik, G. Perepelitsa, A. Israel and A. J. Agranat, " Construction of an Optical Wire Imprinted in Potassium Lithium Tantalate Niobate by $He^+$ Implantation." Appl. Phys. Lett. 92, 191101 (2008).

[14] H. Siman Tov, "MSc thesis at the Hebrew University of Jerusalem" (2008).

[15] R. Fathei, "MSc thesis at the Hebrew University of Jerusalem" (2009).

[16] A. Gumennik, G. Perepelitsa, A. Israel and A. J. Agranat, "A tunable channel waveguide array fabricated by the implantations of $He^+$ ions in an electrooptical KLTN substrate", Optics Express 17, 6166-6176 (2009).

[17] A. Guarino, G. Poberaj, D. Rezzonico, R. Degl'Innocenti and P. Günter, "Electro–optically tunable microring resonators in lithium niobate," Nature Photonics 1, 407 - 410 (2007).